J Mater Sci (2015) 50:4683–4697
DOI 10.1007/s10853-015-9019-8

A comparative analysis of solubility, segregation, and phase formation in atomized and cryomilled Al–Fe alloy powders

Brandon D. Saller[1] · Tao Hu[1,2] · Kaka Ma[1] · Lilia Kurmanaeva[1] · Enrique J. Lavernia[1] · Julie M. Schoenung[1]

Received: 25 February 2015 / Accepted: 9 April 2015 / Published online: 17 April 2015

Abstract Bulk nanostructured and ultrafine-grained binary Al–Fe alloys have been studied in the past for their remarkable strength, hardness, and thermal stability. These properties have been attributed to a combination of solid solution strengthening, precipitate strengthening, and grain boundary strengthening. However, to date, no systematic investigation has been performed to address the factors that govern the evolution of the various metastable and equilibrium precipitates that form as a result of thermal exposure. In this study, Al–2at.%Fe and Al–5at.%Fe powders were synthesized via helium gas atomization and argon gas atomization, respectively. Cooling rates upwards of 10^6 K s^{-1} were achieved resulting in an intermetallic-free starting structure, and a map of the structure as a function of cooling rate was established. Electron backscatter diffraction analysis revealed the presence of a larger number of low-angle grain boundaries relative to high-angle grain boundaries, which influenced nucleation and precipitation of the metastable Al_6Fe phase. Cryomilling of the atomized powder was subsequently performed, which led to grain refinement into the nanometer regime, dispersion of the Fe-containing phases, and forcing of 2at.%Fe into solution within the Al matrix compared to negligible Fe in solution in the as-atomized state. Finally, differential scanning calorimetry was utilized to elucidate the metastable Al_6Fe precipitation temperature (~300 °C) and subsequent phase transformation to the equilibrium $Al_{13}Fe_4$ phase (~400 °C). An activation energy analysis utilizing the Kissinger method revealed three important factors, in order of importance, for ease of Al_6Fe precipitation: segregated regions containing iron, availability of nucleation sites, and the number of diffusion pathways.

✉ Julie M. Schoenung
jmschoenung@ucdavis.edu

Brandon D. Saller
bdsaller@ucdavis.edu

Tao Hu
tahu@ucsd.edu

Kaka Ma
kkma@ucdavis.edu

Lilia Kurmanaeva
lkurmanaeva@ucdavis.edu

Enrique J. Lavernia
lavernia@ucdavis.edu

[1] Department of Chemical Engineering and Materials Science, University of California—Davis, Davis, CA 95616, USA

[2] Department of NanoEngineering, University of California, San Diego, La Jolla, CA 92093, USA

Introduction

The family of Al–Fe alloys is both scientifically and technologically interesting for several reasons. First, the low solubility (0.03 at.%) and diffusivity of Fe in Al (10^{-16} m^{-2} s at 500 °C), as illustrated in the phase diagram in Fig. 1 [1], suggest that the alloys containing these two elements should be thermally stable. The low solubility of Fe in Al has been noted and referenced especially in many studies looking to extend this value via non-equilibrium processing routes [1–5]. Second, published results suggest that there is a range of intermetallic phases, including the metastable orthorhombic Al_6Fe and the equilibrium monoclinic $Al_{13}Fe_4$, for example [5], the formation of which depends on various factors, including thermal and solidification conditions [1, 3, 5–7]. Third, from a sustainability standpoint, both Al and Fe are present in bauxite ore; Al is currently mined from bauxite ore, which is

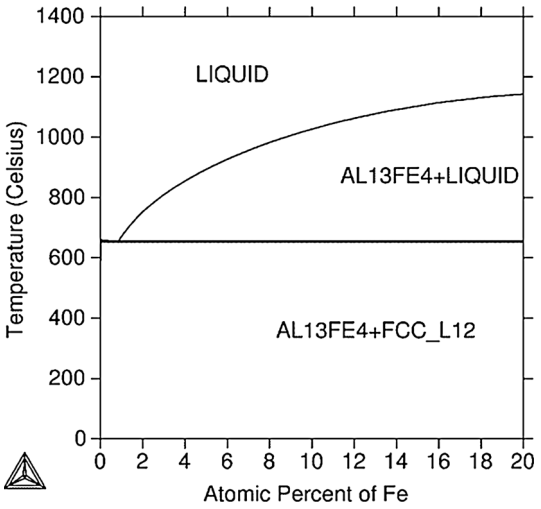

Fig. 1 Binary Al–Fe phase diagram generated with Thermo-Calc® in composition range of interest

composed of alumina and upwards of 30 % Fe-oxide, yet the Fe-oxide is generally discarded as a waste by-product [8]. Fourth, the above-listed characteristics render this system ideal for the development of a family of low-cost, thermally stable materials that can be used in numerous applications [1].

In the past few decades, the study of nanostructured (<100 nm) and ultrafine-grained (~100's nm) Al–Fe alloys has yielded some interesting results. There are numerous published studies on the application of rapid quenching methods, such as melt-spinning [6], e-beam evaporation [9] sputtering [7], mechanical alloying, and severe plastic deformation techniques such as planetary ball milling [3, 5], SPEX® milling [10], and high-pressure torsion (HPT) [11] to fabricate Al–Fe alloys. In related work, Sasaki et al. demonstrated that planetary ball-milled and spark plasma-sintered Al–5at.%Fe can exhibit compressive strengths >1 GPa and significant compressive strain to failure [3]. Subsequent work suggests that these mechanical properties are due to a combination of grain boundary strengthening, load transfer, and Orowan strengthening, with the latter two derived from a range of intermetallic phases including metastable orthorhombic Al_6Fe and equilibrium monoclinic $Al_{13}Fe_4$ [5]. Moreover, these studies almost always report increased (e.g., non-equilibrium) solubility of Fe in Al. Specifically, solid solubility extensions between 2 and 10 at.%Fe in Al have been reported via X-ray diffraction (XRD) analysis [3, 5, 10, 12, 13]. For example, Sasaki et al. [3] used planetary ball milling to process 10 g of Al–5at.%Fe powder for upwards of 150 h and showed via XRD a lack of intermetallic peaks and approximately 3 at.%Fe in solution. Subsequently, phase contrast SEM imaging, however, provided a clear indication of second-phase particles, suggesting a discrepancy in the data [3]. The conditions used in this study, namely an extremely long time and a small amount of powder, suggest that the energy introduced during milling plays an important role in the formation of a non-equilibrium solid solution, although it is clear that more work is required to ascertain this hypothesis. In a related study, Nayak et al. [5] reported what appears to be the highest value of Fe in solution with Al (10 at.%), resulting from the mechanical alloying in a planetary ball mill for 20 h. Binary compositions ranging from 2.5 to 20 at.%Fe in Al were investigated. XRD analysis utilizing the (111) Al diffraction peak was performed with peak shift analysis to support the value of 10 at.%. However, microscopy of the powders was not provided in support of the XRD analysis. Utilizing mechanical alloying of 1–25 at.%Fe in Al in a SPEX® mill, for 20 h, Mukhopadhyay et al. [10] reported 4.5 at.%Fe in solution, as deduced from the (311) Al peak in an XRD pattern. In addition, this study, along with previous ones [3, 5, 10], contradicts the work done by Fadeeva and Leonov [12] regarding the amount of Fe that can be forced into solution (not more than 2 at.%). In the absence of unequivocal microstructural evidence, these apparent contradictions possibly originate from the inappropriate reliance on the presence (or lack thereof) of low-angle intermetallic peaks in Al–Fe XRD patterns. The use of low-angle Al XRD peaks (e.g., Al (111) and Al (311)) for lattice parameter calculations can lead to systematic errors in the value of $\sin\theta$, which leads to error and subsequent erroneous values for the lattice parameter and amount of solute in solution with the matrix [13].

As a result of the low solubility of Fe in Al seen in the phase diagram in Fig. 1, any Fe forced into solution, regardless of the actual value, will eventually precipitate out as the equilibrium $Al_{13}Fe_4$ phase when exposed to elevated temperatures. However, dependent on variations in process conditions, metastable phases can also form. Ball-milled powders, when exposed to temperature, can reveal the formation of both metastable Al_6Fe and Al_5Fe_2 in both the as-milled state and after thermal exposure up to 400 °C, with the Al_6Fe phase being more commonly observed in alloys with less than 10 at.%Fe [3, 5, 10]. Thermodynamically, a phase transformation to equilibrium $Al_{13}Fe_4$ will eventually occur with traditional elevated temperature powder metallurgy-based consolidation methods, typically imparting enough energy to catalyze that transformation [5]. Interestingly, however, and despite numerous published studies on ball-milled Al–Fe alloys, detailed information on the influence of processing conditions on both microstructure and thermal stability of Al–Fe alloys is limited. This lack of fundamental information severely limits our ability to design the microstructure of Al–Fe alloys in order to obtain optimal combinations of physical and mechanical properties.

In view of the above discussion, the present study was motivated by the following questions. First, what is the influence of atomization parameters and milling conditions on the solubility, segregation, and precipitation behavior of Al–Fe alloys? Second, how are these factors influenced by Fe content? To address these questions we implemented the following approach. First, we used high-angle XRD and electron microscopy to measure the amount of Fe forced into solution as a result of two highly non-equilibrium methods, helium powder atomization and cryogenic ball milling. Second, we applied a combination of electron backscatter diffraction (EBSD) and electron microscopy to obtain quantitative microstructural data for two different powder cooling rates and Fe contents; we then related microstructure to subsequent diffusion and phase formation phenomena. Third, we used cryogenic ball milling (cryomilling) in order to limit diffusion-mediated events during the ball milling process to effectively study the role of plastic deformation on phase formation. Finally, thermodynamic analysis via differential scanning calorimetry (DSC) was used to reveal the relative amounts of phases formed as a result of process conditions, in addition to elucidating differences in activation energy for phase formation, to provide insight into the precipitation reactions.

Materials and methods

Material fabrication and processing

The starting materials for atomization in this study were 99.97+ wt% pure Fe pieces and Al–25wt%Fe ingot for the target Al–5at.%Fe and Al–2at.%Fe powders, respectively; each was balanced with 99.9 wt% pure Al ingot to create the target composition. The selection of these two Al–Fe compositions was prompted by the following factors. First, the Al–5at.%Fe composition was selected to provide a comparison to the literature, namely the work done by Sasaki et al. [3]. Second, the Al–2at.%Fe composition was selected based on a conservative upper bound for the amount of Fe that can be forced into the Al matrix, thus creating an intermetallic-free starting structure [12]. Powder was created via two separate gas atomization experiments, the parameters for which are listed in Table 1. Additional information on gas atomization can be found in Ref. [14]. Materials in this condition will be hereafter designated "as-atomized."

Each type of atomized powder was subsequently cryomilled in liquid nitrogen in a modified Szegvari attritor. The parameters used were as follows: stainless steel ball milling media in a 32:1 stainless steel ball-to-powder weight ratio, 180 rpm impeller speed, 12 h milling time, and the use of 0.2 wt% stearic acid ($C_{18}H_{36}O_2$) as a process control agent (PCA) to reduce cold welding of the powder to the balls and vessel, as well as to prevent agglomeration of the powders [15]. For the Al–5at.%Fe material, a 1 kg charge of alloy powder was used, whereas for the Al–2at.%Fe a 500 g charge was used.

Table 1 Gas atomization parameters

Parameters	Al–5at.%Fe	Al–2at.%Fe
Atomization gas	Argon	Helium
Gas pressure (psi)	200	400
Charge (kg)	2.2	2.2
Melt temperature (°C)	1100	1100
Time @ melt temperature (min)	30	30
Nozzle diameter (in/mm)	1/25.4	1/25.4
Powder yield (%)	97.3	46

Chemical analysis of both the as-atomized and cryomilled powders was performed by Luvak Inc. and LECO Corp., using inert gas fusion-ASTM E 1019-08 (for oxygen and nitrogen) and direct current plasma emission spectroscopy-ASTM E 1097-07 for iron.

Material characterization

Thermodynamics and kinetics

A model NETZSCH DSC 404 F3 Pegasus differential scanning calorimeter (DSC) was used for thermal analysis. Alumina crucibles were used in order to mitigate any reaction products between the Al–Fe powder ($\sim$30 mg) and the crucible. Heating was performed from room temperature (25 °C) to 600 °C, with the melt temperature of Al being 660 °C. Heating rates of 5, 10, 20, and 30 °C min^{-1} were used for construction of Kissinger plots [16]. For each sample and heating rate, three DSC runs were performed: one with two empty alumina crucibles, one with an empty alumina crucible and an alumina crucible filled with the powder of interest, and a re-run of the second scan as a sintering and degassing correction step; in this third run, any baked out moisture, gasses and sintering will mostly have occurred already in the second run, thus allowing them to be subtracted out of the final curve. All DSC scans were performed against a standard calibration performed at that heating rate and temperature range, under a protective argon atmosphere.

An equilibrium Al–Fe phase diagram was created with the use of Thermo-Calc® version 5.0 (Thermo-Calc® Software AB, Stockholm, Sweden) over the relevant composition and temperature range values used in this study. This allowed a more appropriate definition for the x-axis (i.e., the range of Fe content) when compared to traditionally published binary Al–Fe phase diagrams.

Phase identification and microstructure

Phase identification of the powders was carried out via XRD using a Scintag X-ray diffractometer equipped with a graphite monochromator using Cu Kα radiation (λ = 0.15406 nm), in order to determine the specific intermetallic phases present, or lack thereof. In addition, an Oxford Instruments Nordlys Nano electron backscatter diffraction (EBSD) detector, equipped to a Phillips XL-30 SFEG scanning electron microscope (SEM), was used for targeted phase identification of intermetallics as well as overall mapping of cross-sectioned powder particles. Cross-sectioning of the powder particles was performed by first mounting the powder particles using conductive (Konductomet) mounting medium mixed with the powder in a Buehler SimpliMet 3000 mounting press. The resulting coupons were subsequently sectioned using a diamond saw into rectangular prism shapes that were then cross-section ion polished with a JEOL SM-09010 cross-section ion polisher for 8 h at 6 kV and 120 μA. Post-processing of the EBSD data was carried out using Oxford Channel 5 software.

Microstructural analysis of cryomilled powder thin foils was accomplished with the use of a Phillips CM-12 transmission electron microscope (TEM) operating at 100 kV, using a tungsten filament, as well as a JEOL JEM-2500SE high-resolution transmission electron microscope (HRTEM) operating at 200 kV. Energy-dispersive X-ray spectroscopy (EDXS) analysis was carried out using a Thermo Fisher Noran System Six on the HRTEM in scanning transmission electron microscopy (STEM) mode. TEM powder samples were prepared by embedding the powder in a resin that was allowed to cure overnight followed by sectioning into 80–90-nm-thick sections using an LKB NOVA microtome with a DiATOME diamond knife. Sections were then placed onto 3.0-mm copper grids with underlying amorphous carbon support.

Heat treatments

Based on data from DSC, heat treatments were performed at temperatures above and below potential precipitation/phase formation exotherms by placing powder in sealed stainless steel vials, and placing the vials into a Thermoline 48000 furnace for 1 h and subsequently quenching in ice water. Heat-treated powder samples were then analyzed by XRD, thus allowing for the identification of phases produced by the exothermic reactions.

Results

Chemical analysis

The target and actual compositions of the powders are shown in Table 2. The conversion from at.%Fe to wt%Fe is 5 at.% = 9.82 wt% and 2 at.% = 4.05 wt%. From that conversion, it can be seen in Table 2 that the Al–5at.%Fe as-atomized powder was within 0.1 wt% of the target Fe composition. Cryomilling led to a 0.5 wt% increase in Fe content as a result of diffusion from the stainless steel balls, as commonly reported for ball-milled alloys. The as-atomized Al–2at.%Fe powder was 0.42 wt% over the target Fe composition, whereas after cryomilling the Fe content increased by 0.07 wt%. For simplicity, the target compositions of Al–5at.%Fe and Al–2at.%Fe will be used hereafter for labeling purposes. Nitrogen was seen to increase in the material due to the use of liquid nitrogen during cryomilling as well as an increase in oxygen and as a result of surface oxidation of the freshly milled powder and the stearic acid PCA, respectively.

Microstructure

Solidification structure of the as-atomized powder

Figure 2 shows backscattered electron/phase contrast SEM images of the as-atomized powder cross-sections. Important to note here is the difference in the solidification structure between the two different powders: fully formed intermetallics in the Al–5at.%Fe (Fig. 2a) material and no intermetallics, yet a structure of segregated Fe, in the Al–2at.%Fe material (Fig. 2b–e). This is a result of the faster cooling rate achieved in the Al–2at.%Fe material which is shown graphically as a function of powder particle diameter in Fig. 3a. In fact, the maximum cooling rate is estimated to be an order of magnitude higher for the Al–2at.%Fe material versus that of the Al–5at.%Fe powder, due to the atomization parameters used. Figure 3b shows the atomized powder diameters obtained by sieving, which highlights a shift in the distribution to smaller powder particle diameters for the Al–2at.%Fe powder.

Cooling rate calculations for Fig. 3a were performed based on the heat balance analysis of Boettinger et al. in an Al–Fe system as follows [17]:

$$\text{Cooling Rate} = \frac{12 \times k_{\text{gas}} \times \Delta T_{\infty}}{c \times d^2}, \quad (1)$$

where k_{gas} is the gas thermal conductivity, ΔT_{∞} is the difference in temperature between the melt particle and the gas, c is the liquid heat capacity per unit volume (2.67 J cm^{-3} K^{-1}), and d is the powder particle diameter. Calculations were based on the powder solidification initiating with heterogeneous nucleation at the powder surface (an assumption that is supported by results in Fig. 2). Gas thermal conductivities of 0.016 W m^{-1} K^{-1} for argon and 0.142 W m^{-1} K^{-1} for helium were used. An assumption of the starting tanks of helium gas and argon gas being at room temperature (25 °C) was also made. Due to the

Table 2 Chemical analysis of the as-atomized and cryomilled powders performed by Luvak Inc. and LECO Corp., using inert gas fusion-ASTM E 1019-08 (for oxygen and nitrogen) and direct current plasma emission spectroscopy-ASTM E 1097-07 for iron

Material	Fe (at.%)	Fe (wt%)	N (wt%)	O (wt%)
As-atomized Al–5at.%Fe	4.93	9.7	0.006	0.161
Cryomilled Al–5at.%Fe	5.1	10.2	0.662	0.329
As-atomized Al–2at.%Fe	2.21	4.47	<0.001	0.199
Cryomilled Al–2at.%Fe	2.25	4.54	0.324	0.636

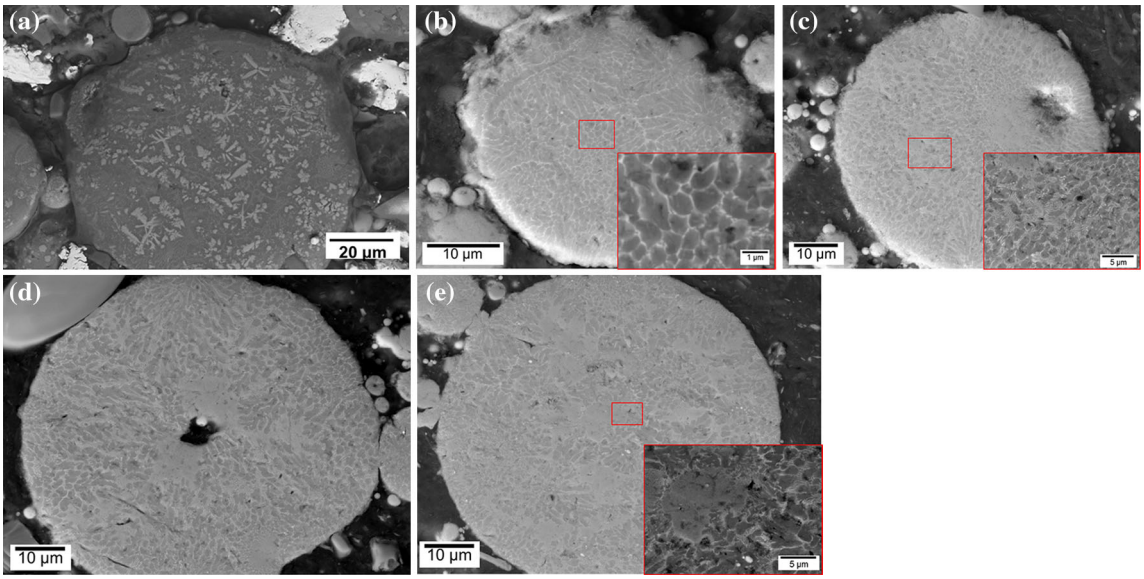

Fig. 2 Cross-sectioned as-atomized powders showing solidification structure via backscatter electron/phase contrast imaging: **a** representative as-atomized Al–5at.%Fe with the structure of fully formed $Al_{13}Fe_4$ intermetallics, **b** 40-μm-diameter Al–2at.%Fe showing α-Al cells bordered with *bright* Fe-rich regions, **c** 60-μm-diameter Al–2at.%Fe showing the addition of an α-Al/Al_6Fe eutectic and a more dendritic structure, **d** 70-μm-diameter Al–2at.%Fe showing an addition of larger regions of segregated Fe, and **e** 85-μm-diameter Al–2at.%Fe with a dominant structure of large Fe-enriched regions (large *lighter gray* regions)

Joule–Thomson effect, the expansion of the gas as it leaves the tank's valve should result in a temperature drop, with the exception of helium due to its Joule–Thomson inversion temperature being much below room temperature [18]. Argon, however, has a Joule–Thomson coefficient of 0.1890 °C atm^{-1} and therefore expands and cools to approximately −4 °C upon exiting a tank at a pressure of 154 atm (2200 psig) [19]. For the sake of completeness and accuracy, these values are provided and included in the analysis. However, the two dominating factors in the cooling rate calculations are found to be, first, the particle diameter and, second, the gas thermal conductivity [17].

Figure 4a shows XRD patterns for the as-atomized powders. The as-atomized Al–5at.%Fe powder shows fully indexed peaks for two intermetallic phases (Fig. 4b): equilibrium, monoclinic $Al_{13}Fe_4$ and metastable, orthorhombic Al_6Fe. In comparison, the as-atomized Al–2at.%Fe powder has a short, broad bump (see the red arrow in Fig. 4) between 42° and 44° 2θ; this bump indicates the weak crystallinity of a phase within the angle range of the strongest reflections for elemental Fe, Al_6Fe, and $Al_{13}Fe_4$. In order to display high Z-contrast, Fig. 5a shows a dark-field STEM image of an approximately 4-μm-diameter powder particle. A particle designated by the yellow arrow indicates a possible heterogeneous nucleation point with a dendritic/cell-like structure radiating outward. These cell-like structures of α-Al are bordered in white as previously seen in Fig. 2b–e, indicating a higher density phase than the surrounding matrix. Figure 5b shows the region marked by the dashed box in Fig. 5a and indicates that these white borders are seen in some places to be made of distinct particles or islands. In Fig. 5c, EDXS analysis is observed across two white cell borders as marked by the dashed line in Fig. 5a. Two Fe peaks are observed corresponding to the boundary positions, as well as a relatively constant Al signal; this analysis provides evidence that the white cell

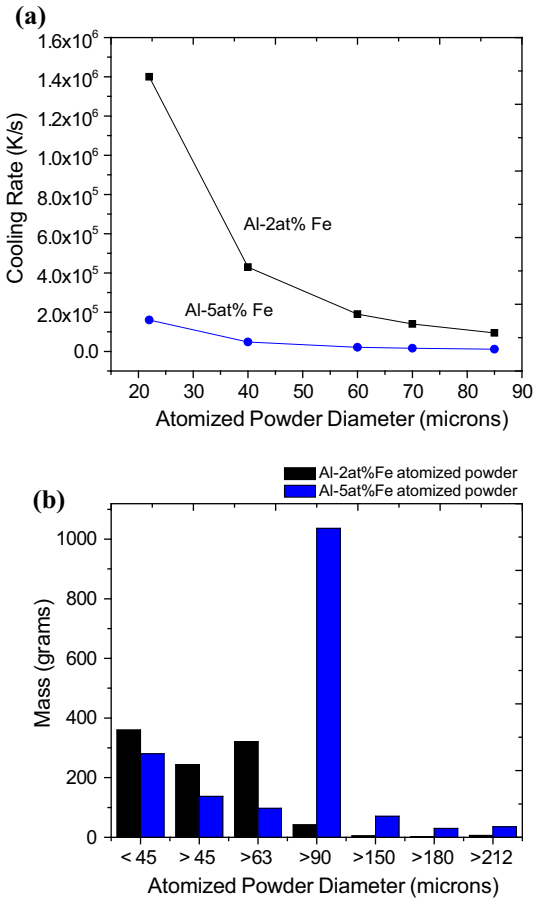

Fig. 3 Effect of atomization gas (argon for Al–5at.%Fe vs. helium for Al–2at.%Fe) on cooling rate and thus atomized powder diameters: **a** calculated cooling rates as a function of powder particle diameter showing higher achievable cooling rates for helium-atomized Al–2at.%Fe, **b** powder diameter histogram showing the effect of higher cooling rates due to helium gas atomization causing a shift in the Al–2at.%Fe particle sizes to less than 90 μm in diameter

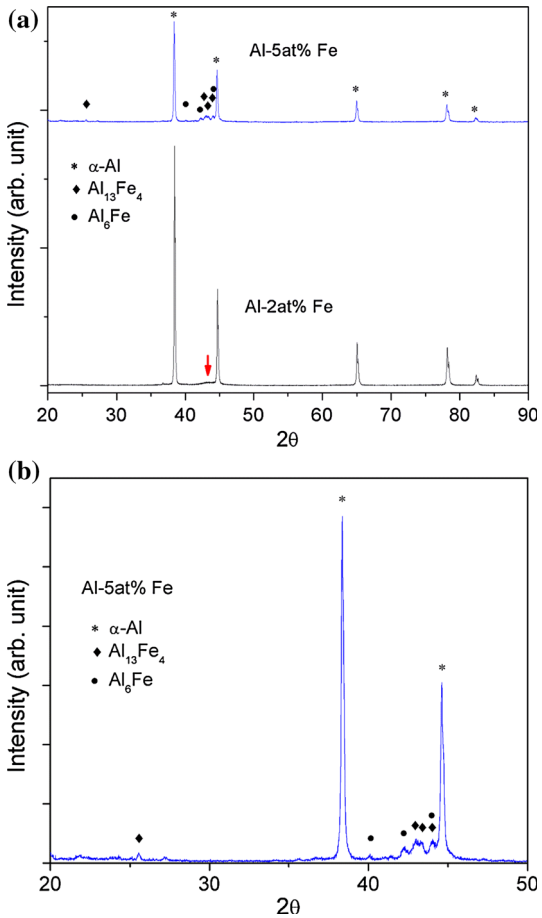

Fig. 4 **a** X-ray diffraction (XRD) of the as-atomized powder and **b** XRD of the as-atomized Al–5at.%Fe powder highlighting the range of 20°–50° 2θ, in order to more clearly distinguish the intermetallic peaks

borders are indeed regions of segregated Fe. An electron diffraction pattern of the powder particle was obtained as shown in Fig. 5d. This pattern indexes as α-Al in the $[1\bar{1}\bar{2}]$ zone axis with no detectable presence of other crystalline phases.

Figure 6 displays maps derived from EBSD using a 150 nm step size and powder particles that are representative of the average particle sizes. Figure 6a, d are band contrast maps, which are gray-scaled to show pattern quality; low-quality areas (grain boundaries, non-indexed points, deformed regions, etc.) are displayed in black, while regions that generated the best-quality Kikuchi patterns approach very light gray/white in color. For both compositions, these maps show a structure within the grains that was not indexed, corresponding mostly to the Fe-segregated regions observed in Figs. 2 and 5 for Al–2at.%Fe, as well as intermetallics in the case of Al–5at.%Fe.

Figure 6b, e are orientation maps with inverse pole figure Z coloring (crystal directions parallel to sample surface normal), high-angle grain boundaries (>15° misorientation) highlighted in black and low-angle grain boundaries (15° > misorientation > 2.5°) highlighted in silver. Powders of both compositions are seen to be crystalline and for particles greater than 5–10 μm in diameter, polycrystalline. The representative 45-μm-diameter Al–2at.%Fe powder particle in Fig. 6b shows an intermetallic-free structure with a large number of high-angle grain boundaries (118 grains). In contrast, the representative 95-μm-diameter Al–5at.%Fe powder particle in Fig. 6e shows that monoclinic $Al_{13}Fe_4$ (displayed in white) is present both at grain boundaries (both high angle and low angle) and within the grains; only 27 grains were present within this particle.

Figure 6c, f are recrystallized fraction maps. This type of map displays deformed grains in red, substructured grains in yellow, and recrystallized grains in blue, which is determined on the basis of the internal average

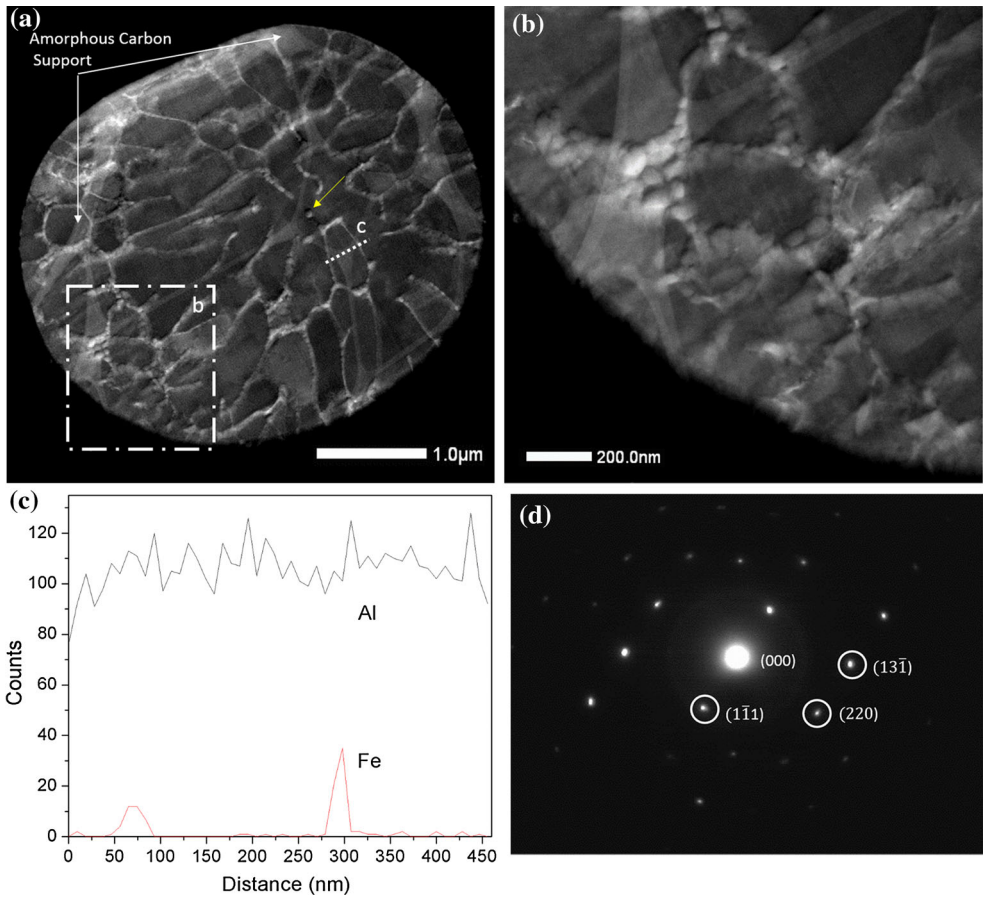

Fig. 5 **a** Scanning transmission electron microscopy (STEM) image of microtomed, as-atomized Al–2at.%Fe powder particle indicating a possible solidification nucleation point with *yellow arrow*, **b** higher magnification image of area indicated by *dashed box* in (**a**), **c** energy–dispersive X-ray spectrometry (EDS) line scan across cell boundary, and **d** electron diffraction pattern of powder particle in [1-1-2] zone axis

misorientation within the grain. If this average misorientation exceeds that of the user-defined value to define a sub-grain (2.5 degrees in this study), then the grain is classified as deformed. If the grain consists of sub-grains for which the average misorientation is under this value, yet the misorientation from grain to grain is between 2.5 and 15 degrees, the grain is classified as substructured. All of the remaining grains are classified as recrystallized [20, 21]. As seen in Fig. 6c, a majority of the Al–2at.%Fe powder particles are recrystallized with most of the rest being substructured; very few deformed regions are observed. In contrast, there is a larger amount of substructure seen in the Al–5at.%Fe powder (Fig. 6f) relative to recrystallized region. Again, a small amount of deformed regions (red) are observed; however, all of the deformed regions are within the $Al_{13}Fe_4$. Figure 6g provides a stacked histogram of the misorientation angle distribution for both compositions. Misorientations between 2.5 and 60 degrees are observed with a much larger presence of low-angle grain boundaries (73 %) in the Al–5at.%Fe powder (red histogram) relative to the Al–2at.%Fe powder (27 %, black histogram).

Cryomilled powder

As a result of severe plastic deformation (SPD) induced by cryomilling, the regions of segregated iron in the Al–2at.%Fe powder were broken up and dispersed as seen in the phase contrast imaging in Fig. 7a. An illustration of the processes at work during cryomilling is also observed in Fig. 7a, namely the crushing of the powder between stainless steel balls, then folding and cold welding of the powder particles. In related studies, the strain energy imparted to the powder, as a result of the high-speed attritor and resulting ball-to-powder collisions, was shown to positively correlate with the amount of grain refinement and the speed of that refinement [22, 23]. Figure 7b is a dark-field STEM image of the same cryomilled Al–2at.%Fe powder. Again, the phases can be distinguished with the denser phase in white (minus the amorphous carbon support film) and the matrix in black/gray. Electron diffraction was carried out (inset Fig. 7b) and showed no presence of any second phase; all rings indexed as aluminum. Dark-field TEM by exciting the partial {111} diffraction ring (Fig. 7c) was performed providing even

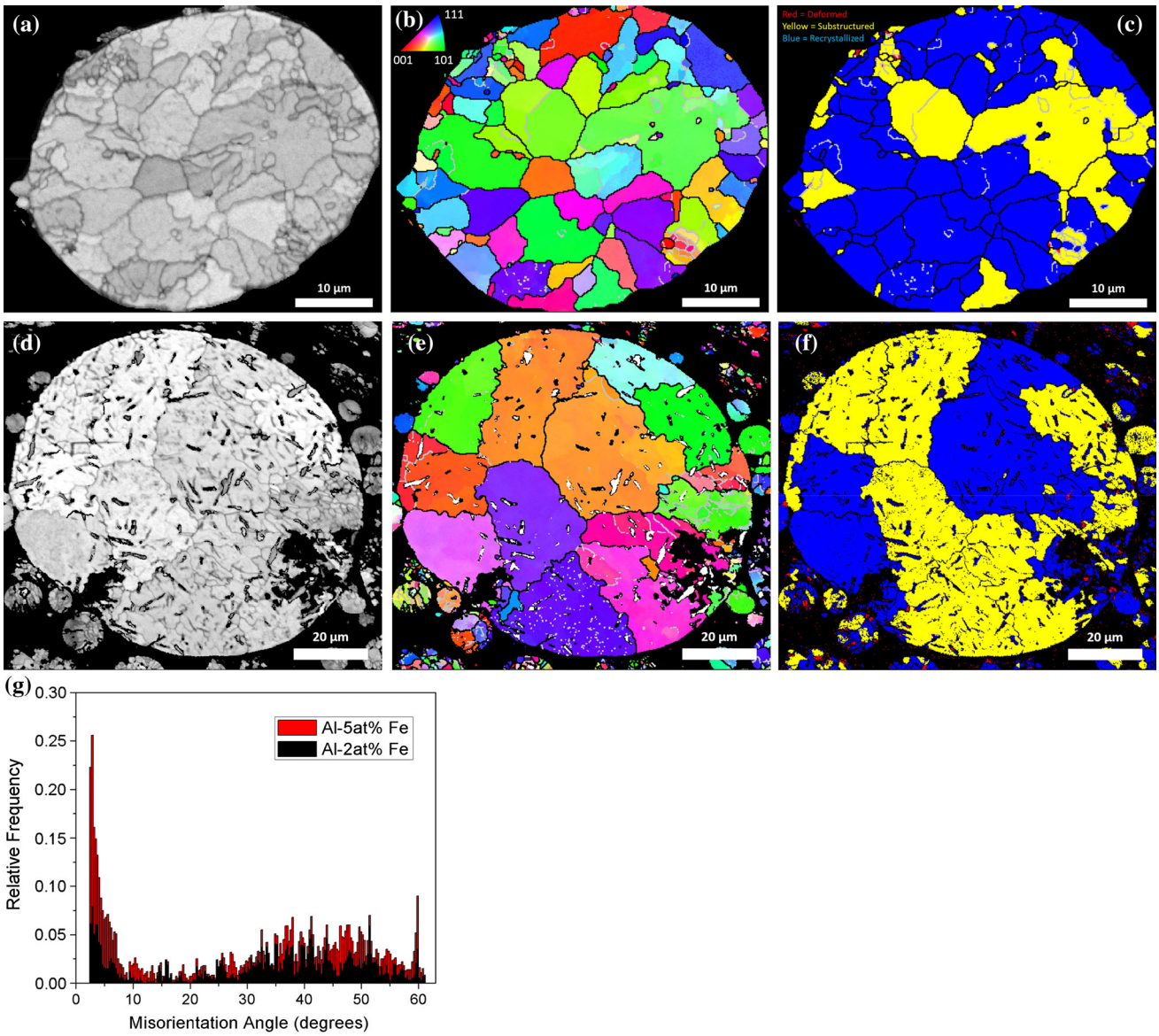

Fig. 6 Electron backscatter diffraction (EBSD) of the as-atomized powders comparing the Al–2at.%Fe **a**–**c** and Al–5at.%Fe **d**–**f** compositions. The step size used for these maps was 150 nm. **a**, **d** Band contrast/pattern quality maps. **b**, **e** Orientation maps with inverse pole figure Z coloring and high-angle grain boundaries in *black* and low-angle grain boundaries in *silver*. The $Al_{13}Fe_4$ phase is shown in *white* for Al–5at.%Fe. **c**, **f** Recrystallized fraction maps [grain boundaries not overlaid in (**f**); refer to (**e**)]. **g** Misorientation distribution for both compositions using stacked bar charts

stronger evidence for the lack of intermetallics and the highly deformed, nanocrystalline nature of the grains. An HRTEM image of the cryomilled Al–2at.%Fe powder, however, shown in Fig. 7d, shows a second-phase particle (indexed as either Al_6Fe or $Al_{13}Fe_4$), in the size range of 5–10 nm, observed sparingly in the microstructure.

Within the cryomilled Al–5at.%Fe powder (Fig. 7e) the pre-existing intermetallic phases were broken up and dispersed within the structure as evidenced by the white particles. This powder was also nanostructured as shown by the inset STEM image in Fig. 7e. Finally, Fig. 7f shows the XRD results for the cryomilled powders. The Al–2at.%Fe pattern shows no distinct second phases, minus a "bump" between 2θ values of 40° and 43°, indicated by the red arrow, as also observed in the as-atomized powder. The Al–5at.%Fe powder, however, shows distinct $Al_{13}Fe_4$ peaks.

Lattice parameters

Before a complete analysis of the phase formation sequence is performed, it is necessary to understand where

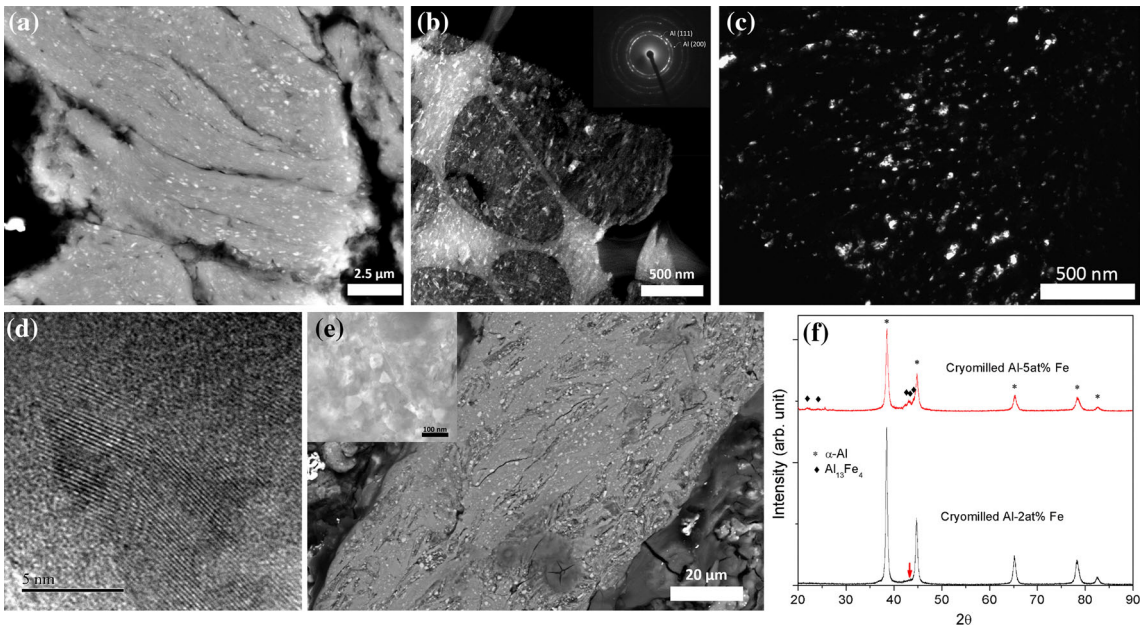

Fig. 7 Cryomilled powder **a** phase contrast (backscattered electrons) SEM image of cross-section ion-polished Al–2at.%Fe powder, **b** *dark-field* scanning transmission electron micrograph (STEM) of microtomed Al–2at.%Fe on amorphous carbon support with *inset* diffraction pattern, **c** *dark-field* TEM of Al–2at.%Fe excited with Al {111} diffraction ring, **d** high-resolution transmission electron micrograph (HRTEM) of cryomilled Al–2at.%Fe powder showing 2nd phase, **e** phase contrast (backscattered electrons) SEM image of Al–5at.%Fe (*inset* bright-field TEM image showing nanocrystalline grains), and **f** X-ray diffraction (XRD) of both Al–2at.%Fe and Al–5at.%Fe cryomilled powders

the Fe resides in the microstructure. XRD patterns in the range of 110°–140° 2θ values were obtained for all four powders. In addition, two XRD scans were run for each material to ensure repeatable results. Lattice parameters, a, were calculated from the XRD patterns using a combined equation of Bragg's Law and geometric relations for an FCC unit cell:

$$a = \frac{\lambda}{2\sin\theta}\sqrt{h^2 + k^2 + l^2}, \tag{2}$$

where $\lambda = 1.5406$ Å for Cu Kα radiation. The highest angle peaks, (Al (331), Al (420), and Al (422)), were chosen for the lattice parameter calculation because the systematic error in $\sin\theta$ decreases as θ increases, resulting in better accuracy [24]. Experimentally obtained lattice parameters were plotted versus $\cos^2\theta/\sin\theta$ as the largest single source of error in XRD is the displacement of the specimen from the diffractometer axis given by

$$\frac{\Delta d}{d} = -\frac{D\cos^2\theta}{R\sin\theta}, \tag{3}$$

where R is the radius of the diffractometer circle and D is the displacement of the specimen surface from the center of the diffractometer [24]. From these plots, a best fit line was extrapolated to the y-axis to obtain the lattice parameter at an effective 2θ of 180° ($\cos^2\theta/\sin\theta$ equals zero), which would represent the minimal obtainable, systematic error; systematic error in the case of this study was reduced to at least 0.15 % using the highest possible angle Al XRD peak: Al (422). The resulting extrapolated lattice parameter values are listed in Table 3. Both the as-atomized powders have a calculated lattice parameter of 0.4050 nm, essentially the same as the value for pure Al. Both the cryomilled powders have lattice parameters of 0.4036 nm, indicating that the smaller Fe atoms are forced into substitutional sites in the Al matrix as a result of cryomilling, thus reducing the lattice parameter. This effect of cryomilling forcing solutes into the matrix lattice (FCC-Al in this case) has been documented in the literature, especially for the case of Mg in Al [25, 26]; however, to the authors' knowledge, this is the first report of a supersaturated solid solution of Fe in Al as a result of cryomilling.

Phase formation

Figure 8 shows DSC results for the four different powders at four different heating rates for subsequent activation energy analysis. The main features of these curves are the two exotherms corresponding to Al_6Fe precipitation at ~300 °C and a phase transformation from metastable

Table 3 Summary of the lattice parameter (a), amount of Fe in solution calculated via XRD, and the powder starting structure as a function of processing

Material	a (extrapolated)	Fe in solution (at.%)	2nd phases present
Pure Al	0.4049	0	None
As-Atomized Al–2at.%Fe	0.4050	0	None
As-Atomized Al–5at.%Fe	0.4050	0	Al_6Fe and $Al_{13}Fe_4$
Cryomilled Al–2at.%Fe	0.4036	2–2.5	(Al_6Fe or $Al_{13}Fe_4$)*
Cryomilled Al–5at.%Fe	0.4036	2–2.5	$Al_{13}Fe_4$

* Very small amount; undetectable by diffraction techniques

Al_6Fe to equilibrium $Al_{13}Fe_4$ at ~400 °C, as verified by XRD after heat treatments were applied at temperatures above and below that of the exotherms. The peak onsets and peak areas (reaction onset and reaction enthalpy, respectively) for a 20 °C min^{-1} heating rate are displayed in Table 4. These values are used later in the phase formation analysis.

Discussion

Atomized powder starting structure

It is of interest to note that helium has ~9 times the thermal conductivity of argon allowing for the observed higher cooling rates (Fig. 3a), in addition to the fact that

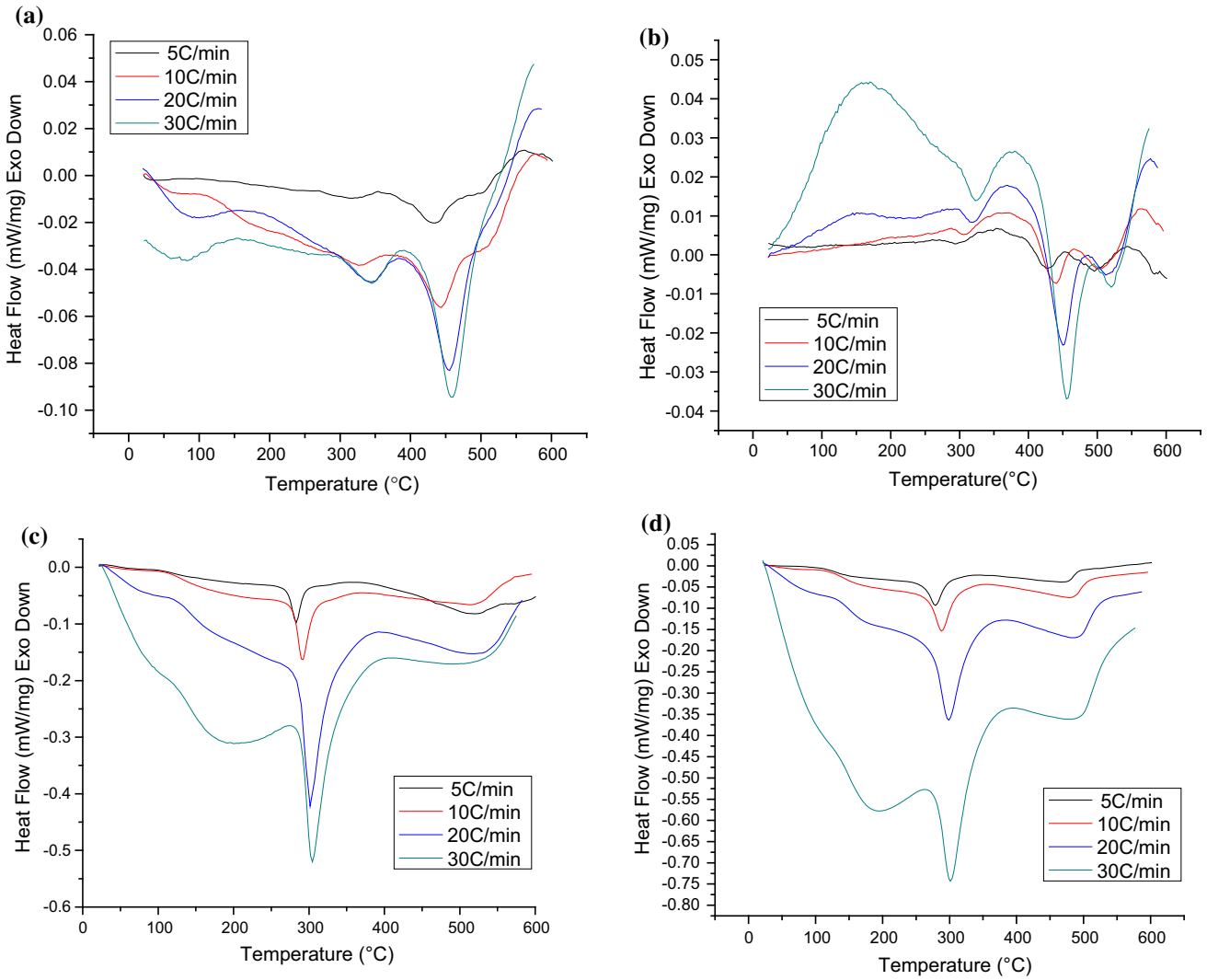

Fig. 8 Differential scanning calorimetry (DSC) **a** as-atomized Al–2at.%Fe, **b** as-atomized Al–5at.%Fe, **c** cryomilled Al–2at.%Fe and **d** cryomilled Al–5at.%Fe

helium can be accelerated much faster than argon because of its molecular weight [27, 28]. As a result, a distribution of smaller particle sizes was observed for the Al–2at.%Fe powder relative to the Al–5at.%Fe powder (Fig. 3b).

Because of the wide size distribution present in the intermetallic-free Al–2at.%Fe powder, it is possible to map the microstructure evolution as a function of cooling rate (i.e., small powder particles cooled faster than large powder particles). Figure 2b–e shows progressively larger 40–85-μm-diameter Al–2at.%Fe powder particles with a structure that has evolved from purely cells to cells + dendrites, followed by the addition of an α-Al/Al_6Fe eutectic [29, 30], and finally the presence of large Fe-enriched regions as observed most prominently in Fig. 2e. This structure agrees with previous reports of the solidification sequence for Al–Fe alloys, of varying composition, as a function of powder particle diameter [17, 31]. In addition, the non-equilibrium nature of this segregated structure is evidenced by the presence of equilibrium $Al_{13}Fe_4$ intermetallics in the Al–5at.%Fe atomized powder (Figs. 2a and 6e) synthesized at a slower cooling rate. As introduced in the Results section, there is evidence in Fig. 2b, d suggesting that the solidification sequence began via heterogeneous nucleation; this suggestion is consistent with other observations in the literature, although it is difficult to prove [32, 33].

Amount of Fe in solution

Extrapolated lattice parameters were compared to a master plot of lattice parameter versus atomic percent Fe to determine the amount of Fe in solution [10]. As seen in Table 3, the extrapolated lattice parameters calculated for both the as-atomized Al–2at.%Fe and Al–5at.%Fe were 0.4050 nm, corresponding to negligible Fe in solution, even though cooling rates upwards of 10^6 K s^{-1} were obtained in the Al–2at.%Fe powder. Subtracting out noise using a baseline for the XRD data, it would be easy to miss the broad bump shown between 40° and 44° 2θ in Fig. 4, indicating a phase with weak crystallinity. Solidification front velocities determined by the cooling rate, and thus external heat extraction during gas atomization, determine the resulting microstructure [14, 17]. As a result, solidification front velocities/cooling rates (Fig. 3a) that were achieved in this study demonstrated the smallest powders to have a microcellular structure (Fig. 2b) that resulted from solute rejection by dendrites during solidification [17]. Less time was available for lateral diffusion of the rejected solute due to the high cooling rates [14]. The highest observed cooling rates in this study, 10^5–10^6 K s^{-1}, agree with the published literature on atomized or melt-spun Al–Fe powder (10^4–10^6 K s^{-1}, respectively) [2] and various other atomized or melt-spun conventional aluminum alloy powders (10^3–10^6 K s^{-1}) [14, 34].

Both the cryomilled powders had extrapolated lattice parameters of 0.4036 nm, corresponding to approximately 2.5 at.% in solution when referencing the master plot derived from the literature (again listed in Table 3) [10]. However, from chemical analysis (Table 2), the composition of the nominal Al–2at.%Fe cryomilled powder is actually approximately Al–2.2at.%Fe. This value falls below the value of 2.5 at.%Fe obtained from the empirically derived master plot due to error/uncertainty in the values the plot is constructed from. Therefore, the amount of Fe in solution is stated here to belong in the range of 2–2.5 at.%Fe, closer to 2at.%Fe, which agrees with preliminary atom-probe tomography data (not included here). Increase in the solid solubility as a result of severe plastic deformation in general can be attributed to the generation of microstructural defects in the form of grain boundaries, vacancies, and high dislocation densities, thus promoting diffusion pathways and sites for solute atoms [35]. Diffusion during traditional mechanical milling is also aided by local rises in temperature. However, milling of powders in this study is carried out in a liquid nitrogen slurry (hence "cryo"milling), and thus diffusion is severely limited/nonexistent due to a very strong dependence of the diffusion coefficient on temperature. This cryogenic temperature allows for accelerated fracturing of the powder particles and subsequent cold welding, while inhibiting recovery, thus opening the way for the introduction of large amounts of defects [36]. Additionally, a minimum grain size model by Mohamed [37] has shown a minimum grain size of 25 nm obtainable by mechanical milling of aluminum powder, with decreases in that minimum grain size as a function of lowered milling temperature and increased

Table 4 Summary of differential scanning calorimetry (DSC) data at 20 °C/min heating rate

Material	Al_6Fe peak onset (°C)	Al_6Fe peak area/reaction enthalpy (J/g)	$Al_{13}Fe_4$ peak onset (°C)	$Al_{13}Fe_4$ peak area/reaction enthalpy (J/g)
As-atomized Al–2at.%Fe	306	−1.10	419	−7.77
As-atomized Al–5at.%Fe	299	−0.382	412	−2.46
Cryomilled Al–2at.%Fe	288	−23.8	401	−23.2
Cryomilled Al–5at.%Fe	277	−23.9	384	−16.9

hardness of the material being milled. This model operates based on a balance between dislocation structure introduced by severe plastic deformation and recovery by thermal processes [37].

Due to the intense plastic deformation of the powder, the microstructure is homogenized as seen in the transition from segregated regions of Fe in the as-atomized Al–2at.%Fe (Fig. 2b–e) to much finer segregated regions in Fig. 7a, and from needle-like $Al_{13}Fe_4$ intermetallics in Fig. 2a to dispersed intermetallics in Fig. 7e, for the as-atomized and cryomilled Al–5at.%Fe, respectively. The cryomilling process creates large surface areas on both the nano- and micro-scale, thus allowing for the non-equilibrium dissolution of Fe into substitutional lattice positions at concentrations upwards of 2at.%Fe, as shown in Table 3. Specifically, with large amounts of grain boundary area introduced as a result of severe plastic deformation during cryomilling, coupled with the introduction of structural defects and local stress, Fe solute atoms can more easily be incorporated into the structure and substitute for the Al matrix atoms [35].

Thermodynamic analysis of precipitation

This study has shown through DSC (Fig. 8) that independent of composition (up to 5 at.%Fe) and processing, the phase formation sequence begins with regions of segregated Fe that then precipitate into metastable Al_6Fe at temperatures of approximately 300 °C (see values in Table 4), and then a phase transformation from metastable Al_6Fe to equilibrium $Al_{13}Fe_4$ occurs at a temperature of approximately 400 °C. However, the energetics behind these reactions are shown to vary as a function of processing route. The precipitation of Al_6Fe is studied in more depth in this paper as it is the most temperature-sensitive phase; Al_6Fe will eventually transform to the equilibrium $Al_{13}Fe_4$ given a high enough temperature [1] as evidenced in this study by the XRD-verified DSC results in Fig. 8. In order to quantify the Al_6Fe precipitation event, three calculations were performed: peak onset identified by a change in slope from the baseline representing the start of the reaction, peak area defining the reaction enthalpy and indicating the amount of phase formed, and the activation energy defining the energy required to start the reaction [38].

Activation energy was calculated based on the Kissinger method which operates under the assumption that the maximum reaction rate occurs at the peak temperature of any given endotherm or exotherm, resulting in the following equation [16]:

$$\frac{d\left(\ln\frac{\phi}{T_P^2}\right)}{d\left(\frac{1}{T_P}\right)} = \frac{-E_A}{R}, \tag{4}$$

where $\varphi = dT/dt$ is the heating rate in K s^{-1}, T_P is the peak temperature in Kelvin, E_A is the activation energy in kJ mol^{-1}, and R is the gas constant (8.314 J $K^{-1}mol^{-1}$). It can be seen that plotting $\ln T_P^2/\varphi$ versus $1/T_P$, for different heating rates, should result in a straight line of a slope E_A/R, thus yielding a value for the activation energy; Fig. 9 shows such a plot for the Al_6Fe precipitation peak, for all four materials, with good linear fit (adjusted $R^2 \geq 0.95$). From this plot, the slope was multiplied by the gas constant giving activation energy values for Al_6Fe precipitation, provided in Table 5. Looking first at the as-atomized powder, the values in Table 5 show that the activation energy for precipitation of Al_6Fe is 7 % higher in the case of Al–2at.%Fe (160 kJ mol^{-1}) versus Al–5at.%Fe (149 kJ mol^{-1}). However, the reaction enthalpy (peak area) is approximately three times larger for Al–2at.%Fe. The enthalpy result can be explained simply by observing the SEM images of the cross-sectioned powder particles in Fig. 2 and the EBSD maps of the particles in Fig. 6. The as-atomized Al–5at.%Fe powder was cooled sufficiently slowly during atomization to allow for the formation of intermetallics, thus consuming a majority of the available Fe. However, the Al–2at.%Fe, being cooled an order of magnitude faster, retained a structure of segregated iron, devoid of any intermetallic phases. This in turn made more Fe available for the formation of more Al_6Fe phase. This phase has been reported in previous studies on rapidly solidified alloys with less than 10 at.%Fe as the first phase formed at a temperature of approximately 300 °C, which is consistent with the work presented in this study [5, 39]. Preferential formation of the Al_6Fe phase over the formation of the equilibrium $Al_{13}Fe_4$ may be explained by the complexity/lack of symmetry of the $Al_{13}Fe_4$ monoclinic

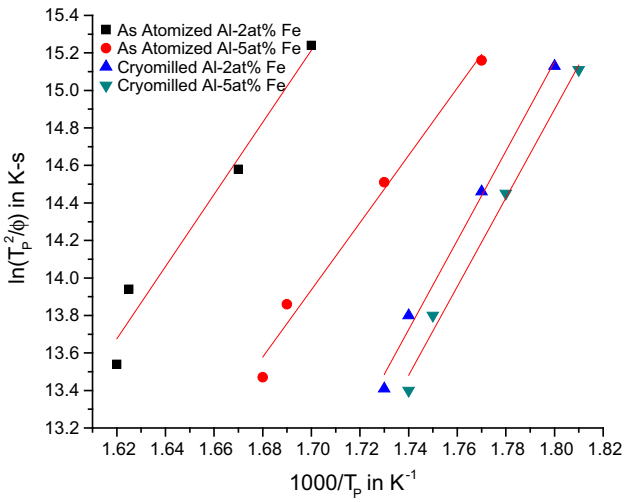

Fig. 9 Kissinger plots utilizing the general Kissinger method for the Al_6Fe differential scanning calorimetry (DSC) exotherm

cell versus the Al_6Fe orthorhombic cell [10], in addition to the larger size of the $Al_{13}Fe_4$ cell having 100 atoms versus Al_6Fe's 28 atoms [1, 40]. A metastable equilibrium state is achieved until enough energy is supplied to overcome the activation barrier for transformation to the equilibrium $Al_{13}Fe_4$ phase.

Grain boundary-assisted diffusion

The reasons for the activation energy being lower for precipitation of Al_6Fe in the as-atomized Al–5at.%Fe versus Al–2at.%Fe are complex. The first main difference between the two as-atomized structures is the obvious presence of intermetallics in the Al–5at.%Fe and lack thereof in the Al–2at.%Fe powder. More advanced microstructural analysis, heretofore unreported in the literature, in the form of EBSD (Fig. 6) was therefore carried out on the as-atomized powder. Comparing the orientation maps (Fig. 6b, e), it is seen that there are generally more grains per powder particle in the Al–2at.%Fe. In fact, as calculated in the results, the number density of grains is approximately 20 times higher in the Al–2at.%Fe powder: 0.0742 grains/μm^2 versus 0.0038 grains/μm^2, respectively (a grain being defined in this case as an ordered array of atoms of one phase separated from another of the same phase by 15° or higher misorientation, i.e., a high-angle grain boundary). Looking at Fig. 6g, which shows the frequency distribution for misorientation angles, it is observed that the as-atomized Al–2at.%Fe powder is composed mostly of high-angle grain boundaries of various misorientations, whereas the Al–5at.%Fe powder has a very large fraction of low-angle grain boundaries. Random high-angle grain boundaries are characterized by poor fit between adjacent grains and thus a more open structure than low-angle grain boundaries [41]. This more open structure traditionally yields good diffusion pathways for solute atoms [42]; coupled with the larger presence of high-angle grain boundaries in the Al–2at.%Fe powder, this would make this powder seem like a more likely candidate for low-activation energy precipitation than the Al–5at.%Fe powder. However, the recrystallized fraction maps in Fig. 6c, f shed more light. A much larger fraction of substructured and deformed regions are observed in the as-atomized Al–5at.%Fe powder than in the Al–2at.%Fe powder. This may be explained due to the $Al_{13}Fe_4$ phase being present, thus pinning the structure and preventing recrystallization [43]. These deformed regions are areas of strain within the material, and the substructured regions consist of low-angle grain boundaries, which, by definition, are arrays of dislocations [41]. These microstructural features, specifically low-angle grain boundaries, present more nucleation sites for precipitation of Al_6Fe than are present in the Al–2at.%Fe as-atomized powder [39]. Therefore, because diffusion of Fe in Al is so minimal (diffusion coefficient (D) of Fe in Al @ 500 °C = 10^{-16} m^2 s^{-1} vs. 10^{-4} m^2 s^{-1} for Al self-diffusion [1]), a large number of diffusion pathways are less significant than a combination of, first, localized Fe-rich regions and, second, nucleation sites for Al_6Fe precipitation.

Cryomilling-induced structural evolution

It is now seen that the starting structure in these powders significantly influences the resulting phase formation. Therefore, it is expected that cryomilling would induce major changes to the powder structure and thus the resulting phase formation. Again referring to Table 4, cryomilled powder is seen to have close to a 20 % higher activation energy for Al_6Fe precipitation than the as-atomized powder, irrespective of composition. To explain this increased activation energy, it is important to discuss two important effects of cryomilling: introduction of impurities and dispersoids, and severe plastic deformation of the structure [25].

The chemical composition of the cryomilled powder is shown in Table 2. One highly cited compositional benefit of cryomilling is the incorporation of nitrogen into the powder [44], which again is observed in Table 2. Nitrogen has been shown to form a hexagonal AlN phase at the grain boundaries and thus act in a Zener pinning mechanism, retarding grain growth and thus increasing the thermal stability of the alloy [44, 45]. These particles, in the powder form, have been estimated to be on the sub-nanometer scale and thus highly difficult to observe via TEM; the volume fraction is also small enough to make it difficult to observe via XRD [44]. In addition to the nitride content, cryomilling breaks up the oxide layer on the surface of the powder particles and incorporates these alumina particles into the microstructure acting as further obstacles to grain boundary mobility and as a diffusion barrier [36].

Table 5 Summary of activation energies derived from Kissinger plots

Material	Activation energy for Al_6Fe precipitation (kJ/mol)
As-atomized Al–2at.%Fe powder	160
As-atomized Al–5at.%Fe powder	149
Cryomilled Al–2at.%Fe powder	198
Cryomilled Al–5at.%Fe powder	196

Cryomilling is a severe plastic deformation process and therefore, by its nature, imposes significant deformation into the material resulting in a high dislocation density. A significant portion of dislocations rearrange into dislocation walls with subsequent sub-cell formation and rotation into high-angle grain boundaries, generating nanocrystalline-sized grains [25]. Consequently, the grain size of both the cryomilled powders was refined to the nano-scale, as observed in Fig. 7. This again introduced many more random high-angle grain boundaries and a larger dislocation density, both of which act as diffusion pathways for mobile solutes in terms of grain boundary diffusion and pipe diffusion [42]. However, as is the case with the as-atomized powder, local concentration of Fe is the key ingredient for easy, or energetically favorable, precipitation of Al_6Fe. This can be understood by Fick's laws whereby a concentration gradient is the driving force for diffusion [41]. As was mentioned earlier, cryomilling is an effective method for dispersion as in the case of oxides, second phases, and hard phases like ceramic reinforcements [25, 35, 46]. As a result, Fig. 7a–c shows that the once segregated structure of Fe in the Al–2at.%Fe has been broken up and well dispersed. In addition, the $Al_{13}Fe_4$ particles present in the as-atomized Al–5at.%Fe powder were broken up and dispersed (Fig. 7e). This dispersion effectively reduces the concentration gradients, thereby reducing the driving force for diffusion relative to the as-atomized powder, partially explaining the observed increase in activation energy.

To explain the very significant increase in reaction enthalpy seen in Table 4 between the as-atomized and cryomilled powders, it is necessary to go back and look at the amount of Fe in solution. As previously mentioned, the enthalpy is indicative of the amount of phase formed [38]. Because of the intense deformation, upwards of 2.5 at.%Fe was forced into solution in the cryomilled powders, as documented in Table 3 and calculated using high-angle XRD peaks. This Fe in solution within the Al matrix is a source for Al_6Fe precipitation upon heating, as demonstrated continuously in the literature [1, 3, 5, 11], in contrast to the as-atomized powder which contained already-formed intermetallics in the case of Al–5at.%Fe and a range of solidification structures and a progression in phase formation that had already occurred in the case of Al–2at.%Fe (Fig. 2).

Lastly, comparing the XRD patterns for the Al–5at.%Fe cryomilled powder (Fig. 7f) and the as-atomized powder (Fig. 4), the $Al_{13}Fe_4$ peaks are stronger in the cryomilled powder. Al_6Fe peaks are also absent from the pattern, while they were present in the as-atomized case. This indicates a deformation-induced phase transformation from the metastable Al_6Fe phase to the $Al_{13}Fe_4$ phase during cryomilling [47].

Conclusions

Al–2at.%Fe and Al–5at.%Fe powders were synthesized via gas atomization using argon and helium gas atomization, respectively. Cooling rates upwards of 10^6 K s^{-1} were achieved resulting in a solidification structure with decreasing cooling rate as follows: α-Al cells bordered with segregated Fe with low crystallinity → cells + dendrites → addition of α-Al/Al_6Fe eutectic → addition of large Fe-enriched regions → fully formed, equilibrium $Al_{13}Fe_4$. EBSD analysis was applied for the first time and demonstrated that a larger fraction of low-angle grain boundaries contributed to Al_6Fe nucleation and precipitation more so than a large fraction of high-angle grain boundaries. Cryomilling was shown to nanostructure the powder and disperse the Fe-containing phases while subsequently forcing 2 at.%Fe into solution compared to negligible Fe in solution in the as-atomized state. Activation energy analysis utilizing DSC and the Kissinger method demonstrated the following order of importance for ease of Al_6Fe precipitation: (1) localized regions/sources of Fe, (2) availability of nucleation sites, and (3) number of diffusion pathways. In addition, metastable Al_6Fe precipitation was observed to occur in all cases upon heating to ~300 °C with a full phase transformation to equilibrium $Al_{13}Fe_4$ at ~400 °C.

Acknowledgements The authors acknowledge helpful EBSD discussions with Scott Sitzman of Oxford Instruments. Dr. Baolong Zheng of UC Davis is thanked for assistance with gas atomization experiments. The assistance with cryomilling by Hanry Yang is greatly appreciated. The authors would like to acknowledge financial support provided by the Office of Naval Research (Grant No. ONR N00014-12-1-0237) with Dr. Lawrence Kabacoff as the program officer.

References

1. Belov NA, Aksenov AA, Eskin DG (2002) Iron in aluminum alloys: impurity and alloying element. CRC Press, Boca Raton
2. Jones H (1969) Observations on a structural transition in aluminium alloys hardened by rapid solidification. Mater Sci Eng 5:1–18. doi:10.1016/0025-5416(69)90077-9
3. Sasaki TT, Ohkubo T, Hono K (2009) Microstructure and mechanical properties of bulk nanocrystalline Al–Fe alloy processed by mechanical alloying and spark plasma sintering. Acta Mater 57:3529–3538. doi:10.1016/j.actamat.2009.04.012
4. Tonejc A (1971) X-ray study of the decomposition of metastable Al-rich Al–Fe solid solutions. Metall Trans 2:437–440. doi:10.1007/BF02663331
5. Nayak SS, Wollgarten M, Banhart J et al (2010) Nanocomposites and an extremely hard nanocrystalline intermetallic of Al–Fe alloys prepared by mechanical alloying. Mater Sci Eng, A 527:2370–2378. doi:10.1016/j.msea.2009.12.044
6. Kim DH, Cantor B (1994) Structure and decomposition behaviour of rapidly solidified Al-Fe alloys. J Mater Sci 29:2884–2892. doi:10.1007/BF01117597

7. Cantor B, Cahn RW (1976) Precipitation of equilibrium phases in vapour-quenched Al–Ni, Al–Cu, and Al–Fe alloys. J Mater Sci 11:1066–1076. doi:10.1007/BF00553114
8. Liu W, Yang J, Xiao B (2009) Application of Bayer red mud for iron recovery and building material production from alumosilicate residues. J Hazard Mater 161:474–478. doi:10.1016/j.jhazmat.2008.03.122
9. Sasaki H, Kita K, Nagahora J, Inoue A (2001) Nano-metals I. nanostructures and mechanical properties of bulk Al–Fe Alloys prepared by electron-beam deposition. Mater Trans 42:1561–1565. doi:10.2320/matertrans.42.1561
10. Mukhopadhyay DK, Suryanarayana C, Froes FH (1995) Structural evolution in mechanically alloyed Al–Fe powders. Metall Mater Trans A 26:1939–1946. doi:10.1007/BF02670665
11. Cubero-Sesin JM, Horita Z (2012) Mechanical properties and microstructures of Al–Fe alloys processed by high-pressure torsion. Metall Mater Trans A 43:5182–5192. doi:10.1007/s11661-012-1341-z
12. Fadeeva VI, Leonov AV (1992) Formation of Al–Fe supersaturated solid solution by mechanical alloying. Mater Sci Forum 88:481–488
13. Fadeeva VI, Leonov AV, Khodina LN (1995) Metastable phases in mechanically alloyed Al–Fe system. Mater Sci Forum 179:397–402
14. Zheng B, Lin Y, Zhou Y, Lavernia EJ (2009) Gas atomization of amorphous aluminum powder: part II experimental investigation. Metall Mater Trans B 40:995–1004. doi:10.1007/s11663-009-9277-4
15. Lu L (1997) Mechanical alloying. Springer, Berlin
16. Kissinger H (1956) Variation of peak temperature with heating rate in differential thermal analysis. J Res Natl Bureau Stand 57:217–221
17. Boettinger WJ, Bendersky L, Early JG (1986) An analysis of the microstructure of rapidly solidified Al-8 wt pct Fe powder. MTA 17:781–790. doi:10.1007/BF02643853
18. Roy B (2002) Fundamentals of Classical and Statistical Thermodynamics. Wiley, West Sussex
19. Forsythe W (1954) Smithsonian physical tables, 9th edn, vol 120. Smithsonian Institution, Washington
20. Lu H, Sivaprasad P, Davies CHJ (2003) Treatment of misorientation data to determine the fraction of recrystallized grains in a partially recrystallized metal. Mater Charact 51:293–300. doi:10.1016/j.matchar.2004.01.005
21. Tarasiuk J, Gerber P, Bacroix B (2002) Estimation of recrystallized volume fraction from EBSD data. Acta Mater 50:1467–1477. doi:10.1016/S1359-6454(02)00005-8
22. Sun Y, Kulkarni K, Sachdev AK, Lavernia EJ (2014) Synthesis of gamma-TiAl by reactive spark sintering of cryomilled Ti and Al powder blend, part 1: influence of processing and microstructural evolution. Metall Mater Trans A 45A:2750–2758
23. Koch CC (1993) The Synthesis and structure of nanocrystalline materials produced by mechanical attrition: a review. Nanostruct Mater 2:109–129
24. Suryanarayana C, Grant Norton M (1998) X-ray diffraction: a practical approach. Plenum Press, New York
25. Witkin DB, Lavernia EJ (2006) Synthesis and mechanical behavior of nanostructured materials via cryomilling. Prog Mater Sci 51:1–60. doi:10.1016/j.pmatsci.2005.04.004
26. Han BQ, Zhang Z, Lavernia EJ et al (2004) Mechanical behavior of a cryomilled nanostructured Al-7.5 pct Mg alloy. Metall Mater Trans A 35:947–949. doi:10.1007/s11661-004-0019-6
27. Anderson JD (2003) Modern compressible flow, 3rd edn. McGraw-Hill, New York
28. Dykhuizen RC, Smith MF (1998) Gas dynamic principles of cold spray. J Therm Spray Tech 7:205–212. doi:10.1361/105996398770350945
29. Hughes IR, Jones H (1976) Coupled eutectic growth in Al-Fe alloys. J Mater Sci 11:1781–1793. doi:10.1007/BF00708256
30. Adam CM, Hogan LM (1975) Crystallography of the Al–Al_3 Fe eutectic. Acta Metall 23:345–354. doi:10.1016/0001-6160(75)90127-3
31. Cardoso K, Escorial AG, Lieblich M, Botta FW (2001) Amorphous and nanostructured Al–Fe–Nd powders obtained by gas atomization. Mater Sci Eng, A 315:89–97. doi:10.1016/S0921-5093(01)01197-2
32. Groza JR, Shackelford JF, Lavernia EJ, Powers MT (2007) Materials processing handbook. CRC Press, Boca Raton
33. Lavernia EJ, Wu Y (1996) Spray atomization and deposition. Wiley, West Sussex
34. Pickens JR (1981) Aluminium powder metallurgy technology for high-strength applications. J Mater Sci 16:1437–1457. doi:10.1007/BF00553958
35. Suryanarayana C (2001) Mechanical alloying and milling. Prog Mater Sci 46:1–184. doi:10.1016/S0079-6425(99)00010-9
36. Lavernia EJ, Han BQ, Schoenung JM (2008) Cryomilled nanostructured materials: processing and properties. Mater Sci Eng, A 493:207–214. doi:10.1016/j.msea.2007.06.099
37. Mohamed FA (2003) A dislocation model for the minimum grain size obtainable by milling. Acta Mater 51:4107–4119. doi:10.1016/S1359-6454(03)00230-1
38. Hohne G, Hemminger WF, Flammersheim H-J (2003) Differential scanning calorimetry, 2nd edn. Springer, New York
39. Tonejc A (1971) X-ray study of the decomposition of metastable Al-rich Al–Fe solid solutions. Metall Trans 2:437–440. doi:10.1007/BF02663331
40. DE Laughlin, Hono K (2014) Physical metallurgy, 5th edn. Elsevier, Amsterdam
41. Callister WD Jr (2007) Materials science and engineering an introduction, 7th edn. Wiley, New York
42. Porter DA, Easterling KE, Sherif MY (2009) Phase transformations in metals and alloys, 3rd edn. CRC Press, Boca Raton
43. Humphreys FJ, Hatherly M (2004) Recrystallization and related annealing phenomena, 2nd edn. Pergamon, Oxford
44. Hashemi-Sadraei L, Mousavi SE, Vogt R et al (2012) Influence of nitrogen content on thermal stability and grain growth kinetics of cryomilled Al nanocomposites. Metall Mater Trans A 43:747–756. doi:10.1007/s11661-011-0882-x
45. Li Y, Liu W, Ortalan V et al (2010) HRTEM and EELS study of aluminum nitride in nanostructured Al 5083/B4C processed via cryomilling. Acta Mater 58:1732–1740. doi:10.1016/j.actamat.2009.11.015
46. Ye J, Han BQ, Schoenung JM (2006) Mechanical behaviour of an Al–matrix composite reinforced with nanocrystalline Al-coated B4C particulates. Philos Mag Lett 86:721–732. doi:10.1080/09500830600986109
47. Shabashov VA, Brodova IG, Mukoseev AG et al (2007) Deformation-induced phase transformations in the Al–Fe system under intensive plastic deformation. J Phys: Condens Matter 19:386222. doi:10.1088/0953-8984/19/38/386222